



# Compositional evolution of Q-phase precipitates in an aluminum alloy

Aniruddha Biswas<sup>a,b</sup>, Donald J. Siegel<sup>c,\*</sup>, David N. Seidman<sup>a,d</sup>

<sup>a</sup> Department of Materials Science and Engineering, Northwestern University, 2220 Campus Drive, Evanston, IL 60208, USA

<sup>b</sup> Glass & Advanced Materials Division, Bhabha Atomic Research Centre, Mumbai 400085, India

<sup>c</sup> Mechanical Engineering Department, University of Michigan, 2350 Hayward St, Ann Arbor, MI 48109-2125, USA

<sup>d</sup> Northwestern University Center for Atom-Probe Tomography, Northwestern University, Evanston, IL 60208, USA

Received 16 December 2013; received in revised form 30 April 2014; accepted 3 May 2014

## Abstract

Lightweight, age-hardenable aluminum alloys are attracting increasing attention as a means to reduce vehicle mass and improve fuel economy. To accelerate the adoption of these alloys, knowledge of the complex precipitation processes that underlie their primary strengthening mechanism is essential. Here we employ a combination of atom-probe tomography (APT), differential scanning calorimetry (DSC), transmission electron-microscopy, X-ray diffraction and first-principles calculations to reveal the compositional evolution of Q-phase precipitates in a commercial, age-hardenable aluminum alloy, W319. Three different aging conditions are investigated: 438 K/8 h, 463 K/8 h and 533 K/4 h. Co-precipitation of  $\theta'$ - and Q-phase precipitates is observed for all aging conditions, which, when combined with DSC analysis of the precipitation sequence, suggests that Q-phase precipitates serve as heterogeneous nucleation sites for  $\theta'$ -platelets. Regarding composition evolution, aging at the lower temperatures yields Q-phase precipitates that are Cu-rich, yet deficient in Mg and Si: 44Al–22Cu–16Mg–16.5Si at.%. The composition evolves to become Mg-rich after aging at 533 K: ~28Al–9Cu–37Mg–26Si at.%. APT provides evidence for partitioning of Zn to the Q-phase precipitates. The energetics of Zn partitioning was evaluated using first-principles calculations, and suggests that this partitioning is a kinetic effect. Our analyses provide new insights into the complex precipitation processes in commercial Al alloys, and should foster the enhancement of alloy performance through optimization of aging conditions.

© 2014 Acta Materialia Inc. Published by Elsevier Ltd. All rights reserved.

**Keywords:** Atom-probe tomography; Q-phase precipitates; First-principles calculations; Focused-ion beam (FIB) machining; Aluminum alloys

## 1. Introduction

Lightweight, age-hardenable alloys such as aluminum are of growing interest in the transportation sector, where their use has the potential to reduce vehicle mass and thereby improve fuel economy. To facilitate this transition, knowledge of the thermal, temporal and compositional evolution of precipitate phases in these alloys is essential, as precipitation can contribute significantly to the strength of these systems. W319 is one such multi-component commercial alloy that is widely used in the automobile industry

for engine blocks and related applications [1,2]. This complex heat-treatable cast alloy contains at least six different elements, with Si and Cu being the dominant components, Table 1. The Si concentration in W319 can be as high as 7.38 at.% and is known to improve its castability [3]. As in the case of the Al–Cu binary system, the primary metallurgical focus in W319 has been the elucidation of the properties of the ordered metastable  $\theta'$ -phase, which imparts the largest strengthening effect of any phase in its precipitation sequence [4,5]. The  $\theta'$ -phase has a body-centered-tetragonal crystal structure with the stoichiometry  $\text{Al}_2\text{Cu}$ , and  $\theta'$ -precipitates have a platelet morphology with coherent  $(001)_{\theta'} \parallel \{001\}_{\alpha\text{-Al}}$  interfaces parallel to their broad faces.

\* Corresponding author.

E-mail address: [djsiege@umich.edu](mailto:djsiege@umich.edu) (D.J. Siegel).

Table 1

Typical bulk chemical composition of W319 as determined by optical emission spectroscopy.

	Si	Cu	Fe	Mg	Mn	Zn
wt.%	7.48	3.53	0.35	0.31	0.26	0.13
at.%	7.38	1.54	0.17	0.35	0.13	0.05

In addition to  $\theta'$ , a second precipitate phase commonly present in W319 is the equilibrium Al–Mg–Si–Cu quaternary or so-called “Q-phase”. The Q-phase is also observed in a variety of Cu containing 6xxx alloys [6–8] and 2xxx alloys [9,10]. Although its position within the precipitation sequence of W319 is unknown, Q-phase precipitation has been reported to precede  $\theta'$ -precipitation in the case of 2014 Al-matrix composites [10]. Additionally, there have been reports of Q-phase precipitates in dispersion-strengthened Al-based powder metallurgy alloys and Al-matrix composites [10–12]. In spite of its common occurrence, the strengthening contribution of this precipitate to W319 is unknown [5].

The earliest reference to the Q-phase appears to be by Dix et al. [13]. The Q-phase is generally known to have a hexagonal crystal structure with lattice constants  $a = 10.35\text{--}10.40 \text{ \AA}$  and  $c = 4.02\text{--}4.05 \text{ \AA}$  [8,14,15]. Arnberg and Aurivillius [14] determined the crystal structure using single-crystal X-ray diffraction and suggested P-6 as the space group. Weatherly et al. [8] later confirmed this space group using electron diffraction. The related Q'-phase is a coherent or semi-coherent version of the Q-phase having essentially the same crystal structure with slightly different lattice parameters [6,8,15,16]. We note that Al–Mg–Si ternary alloys often contain another precipitate with the same crystal structure and lattice parameters as the Q-phase, but without any Cu; this particular precipitate is variously referred to as B', M, type-C,  $\beta'_C$ , etc. [16–19]. The Q-phase is also occasionally referred to as  $\lambda$ ,  $W$  or  $h$  [10,16,20,21].

Q-phase precipitates usually exhibit a lath or needle-like morphology [5]. Typical dimensions of Q-phase precipitates, depending upon the aging conditions, are reported to be in the range of 2.0–5.0 nm<sup>2</sup> in cross-section and 60–100 nm in length [7]. The long axis of these precipitates is known to be parallel to  $\langle 100 \rangle_{\alpha\text{-Al}}$ , and  $\{150\}_{\alpha\text{-Al}}$  is generally accepted as the habit plane [7,16]. Details of some of the earlier research on this phase can be found in papers by Weatherly et al. [8] and Chakrabarti and Laughlin [16].

Despite the presence of Q-phase precipitates in commercial Al alloys, information about this phase – especially concerning its chemical composition – is at best conflicting. For example, several different values of the stoichiometric composition of the Q-phase have been reported in the literature [8,15]: Al<sub>5</sub>Cu<sub>2</sub>Mg<sub>8</sub>Si<sub>6</sub> (23.8Al–9.5Cu–38.1Mg–28.6Si at.%) [21,22]; Al<sub>4</sub>Cu<sub>2</sub>Mg<sub>8</sub>Si<sub>7</sub> (19.1Al–9.5Cu–38.1Mg–33.3Si at.%) [14]; Al<sub>4</sub>Cu<sub>1</sub>Mg<sub>5</sub>Si<sub>4</sub> (28.6Al–7.1Cu–35.7Mg–28.6Si at.%) [23]; and Al<sub>3</sub>Cu<sub>2</sub>Mg<sub>9</sub>Si<sub>7</sub> (14.3Al–9.5Cu–42.9Mg–33.3Si at.%) [15]. Mondolfo [23] reported the additional compositional variant: 17.2Al–8.9Cu–40.1Mg–33.8Si

[24,25]. These studies were mostly based on analyses of bulk alloys, whereas first-principles calculations were used in Ref. [15]. In another study, Gupta et al. [25] used electrolytic extraction and reported a composition that was essentially the same as reported in Ref. [24]: 18.4Al–9.4Cu–40.1Mg–32.1Si.

The uncertainty in the chemical composition of the Q-phase, especially in precipitate form, has been previously noted [8,15,16]. Nevertheless, only a few experimental studies of Q-phase precipitates have been reported [26–28]. As a result, the composition of this precipitate is debatable and little is known about its compositional evolution with aging temperature. Cayron et al. [26] reported the composition Al<sub>5</sub>Cu<sub>2</sub>Mg<sub>8</sub>Si<sub>6</sub> (23.8Al–9.5Cu–38.1Mg–28.6Si at.%) for the Q-phase in an Al–4Cu–1Mg–Ag wt.% alloy reinforced by SiC particles. Matsuda et al. [27] observed a mean chemical composition of Al<sub>4</sub>Cu<sub>1</sub>Mg<sub>6</sub>Si<sub>6</sub> (23.5Al–5.9Cu–35.3Mg–35.3Si at.%) for Q'-phase precipitates in an Al–1.0Mg<sub>2</sub>Si–0.5Cu mass% alloy. Subsequently, Matsuda et al. [28] presented qualitative evidence for Cu segregation at the  $\alpha\text{-Al}/\text{Q}'$  interface using energy-filtered transmission electron microscopy (TEM) in the Al–Mg–Si–Cu system.

In general, the nanometer scale dimensions of these fine precipitates make quantitative analytical electron microscopy analyses challenging and susceptible to considerable uncertainties. Sagalowicz et al. [17] discussed this problem in their analyses of precipitates in an Al–Mg–Si ternary alloy. They identified the following three reasons for experimental uncertainties involved in energy dispersive X-ray spectroscopy (EDS) analyses: (1) the probe diameter is of the same order of magnitude as the precipitate cross-section, and thus the Al concentration of the precipitate cannot be determined; (2) overlap between the K-edges of the three elements owing to their similar atomic numbers; and (3) fluorescence of the Mg radiation by Si.

An alternative to TEM is modern atom-probe tomography (APT), which is immune to these problems, and is currently the most suitable technique at the sub-nano-to-nanometer scale for studying the composition of fine precipitates. Early reports used one-dimensional atom-probe field-ion microscopy (APFIM) to examine the early stages of precipitation as well as the precipitation sequence in Al–Mg–Si alloys, such as 6061 [29–31]. A Mg/Si ratio close to unity was observed in clusters present in the early stages of precipitation and this ratio remained unchanged throughout the precipitation sequence: co-clusters of Si and Mg  $\rightarrow$  small precipitates  $\rightarrow \beta'' \rightarrow B'$  [30]. This is, to some extent, consistent with the ratio reported for clusters that serve as a precursor to the Q-phase in SiC-reinforced Al–Cu–Mg–Ag alloys [26]. More recently, we have employed APT to study the compositional evolution of  $\theta'$ -precipitates and segregation at  $\alpha\text{-Al}/\theta'$ -interfaces, both coherent and semi-coherent interfaces in Al–Cu alloys and W319 [32,33]. To date, the only study involving an APT analysis of Q-phase precipitates is by Hwang et al. [34]. In their study the effect of Mg on the properties of a 319-type Al-alloy were examined for one aging condition

(T6, 463 K for 8 h). The composition of the Q'-phase precipitates was reported to be  $\text{Al}_4\text{Cu}_2\text{Mg}_8\text{Si}_7$  (19.1Al–9.5Cu–38.1Mg–33.3Si at.%).

The presence of Q-phase precipitates in several commercial Al alloys, combined with the limited – and at times contradictory – information regarding its properties, motivates us to revisit the evolution of these precipitates in detail. In the present study we correlatively apply local-electrode atom-probe (LEAP) tomography, differential scanning calorimetry (DSC), X-ray diffraction, TEM and first-principles calculations to explore the composition, precipitation sequence and co-precipitation properties of Q-phase precipitates in the multi-component prototype alloy W319. Our thermal analysis results reveal the following precipitation sequence in W319 for the aging conditions considered: Guiner–Preston (GP) zones  $\rightarrow$  Q  $\rightarrow$  Q +  $\theta'$ . Aging at the lower two temperatures (438 and 463 K) yields Q-phase precipitates that are Cu-rich but deficient in Mg and Si, with an overall composition of approximately 44Al–22Cu–16Mg–16.5Si at.%. The composition evolves to be Mg-rich after aging at 533 K for 4 h:  $\sim$ 28Al–9Cu–37Mg–26Si at.%. In addition to compositional evolution, we also explore co-precipitation of Q with  $\theta'$ -platelets, and partitioning of solutes to Q-phase precipitates. Our analyses reveal evidence for significant partitioning of Zn to the cores of Q-phase precipitates. Co-precipitation of  $\theta'$  and Q-phase precipitates is observed for all aging conditions, suggesting that Q-phase precipitates could play a role in the nucleation of  $\theta'$ -precipitates. Additionally, first-principles calculations reveal that kinetic limitations are responsible for the observed Zn partitioning to Q-phase precipitates. Our analysis provides atomic-scale insight into the complex precipitation process in multi-component Al alloys, and should enable further improvements to alloy properties through optimization of aging conditions.

## 2. Methodology

### 2.1. Experimental methods

Ford Motor Company (Dearborn, Michigan) provided samples of the commercial W319 alloy. This 319-type alloy differs in composition from the Aluminum Association 319 composition in terms of the Si, Fe, Mg and Mn specified limits [35]. Table 1 displays the bulk chemical composition of W319, obtained using optical emission spectroscopy. Samples were homogenized in air at 758 K for 24 h, followed by water quenching, and then aged in air at 438, 463 and 533 K for 8, 8 and 4 h, respectively. These aging conditions encompass the upper and lower temperature limits typically used to examine precipitation in Al–Si–Cu alloys (463–533 K, see Ref. [5] as an example). Furthermore, a lower temperature condition (438 K) is included to capture the early stages of precipitation. A solutionizing treatment for 24 h at 758 K for this commercial alloy, which is also practiced industrially, is found optimal in our analysis. We have calculated the time required to

reduce a composition fluctuation to 5% of its initial value, and the estimated time at 758 K for all four major elements in this alloy is well within 24 h (Appendix A). We do not make a distinction between Q- and Q'-phase precipitates and refer to them collectively as Q-phase precipitates because the differences between their structures and compositions are insignificant.

Thermal analyses of the W319 samples were performed for the as-solutionized condition and after aging at different temperatures. A Mettler-Toledo DSC was used in an argon atmosphere at a heating rate of  $10 \text{ K min}^{-1}$ . A high-purity Al reference disc was employed to improve the sensitivity of the DSC experiments [36].

Aged samples were characterized by powder diffraction using synchrotron radiation at the Advanced Photon Source (APS), Argonne National Laboratory, at the Dow-Northwestern-DuPont (DND) beam line. Synchrotron radiation with an energy of 17.477 keV and a wavelength of 0.07094 nm was utilized.

Specimens for TEM were prepared by punching discs with a 3 mm diameter from thin foils with a thickness of  $\sim$ 200  $\mu\text{m}$ , followed by grinding with 600-grit SiC paper to a thickness of  $\sim$ 70  $\mu\text{m}$ , dimpling and ion milling using a Gatan Precision Ion Polishing System (PIPS). Conventional TEM was performed employing a JEOL 2000FX microscope at 200 kV. Bright-field images were obtained with the foils oriented slightly off the  $\langle 100 \rangle_{\alpha\text{-Al}}$  zone axis to optimize the contrast between the matrix and the precipitates. High-resolution TEM images of selected samples were obtained using an aberration-corrected FEI Titan high-resolution TEM with specimens oriented along the  $\langle 100 \rangle_{\alpha\text{-Al}}$  zone axis.

Prior to electropolishing, APT sample blanks with a square cross-section of  $\sim 300 \times 300 \mu\text{m}^2$  and 1 cm length were prepared from a W319 sample [37,38]. Several different electropolishing procedures for making sharp needle-shaped specimens from these blanks were attempted, Table 2. But different phases in W319 demonstrate differential electropolishing behavior:  $\alpha$ -Al matrix gets electropolished, whereas Si remains virtually unaffected. Alloy W319 has a very high Si concentration (7.38 at.%), which is beyond the solubility limit of Si in Al (1.5 at.% at the eutectic temperature, 840 K, and the solubility decreases to as small as 0.05 at.% at 573 K [39]). As a result, the excess Si appears as eutectic Si, which is essentially pure Si because the solubility of Al in Si is also small (0.016 at.% at 1463 K): see the scanning electron microscopy micrograph in Fig. 1b. We conclude that

Table 2  
Different electropolishing conditions utilized for our attempts to utilize electropolishing to make APT microtips from W319.

	Electrolyte	Cathode
1	10% perchloric in acetic acid	Stainless steel
2	2% perchloric in butoxyethanol	Stainless steel
3	3.5% perchloric in methanol and glycerin	Aluminum
4	Nitric acid and deionized water	Stainless steel

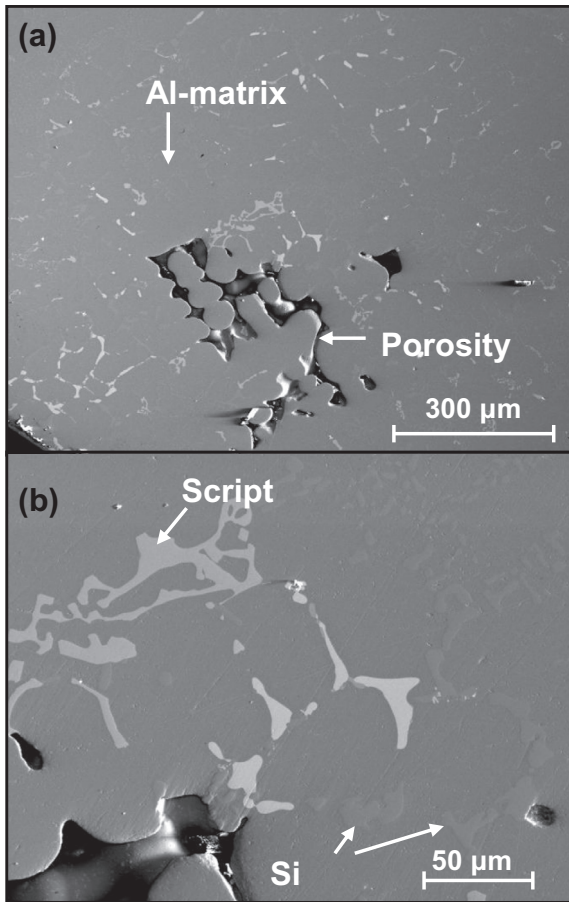


Fig. 1. Typical dendritic cast microstructures of W319: (a) low-magnification micrograph showing Al matrix and porosity; and (b) higher-magnification micrograph showing the script phase and eutectic silicon.

Table 3

Analysis of co-precipitation of the  $\theta'$ - and Q-phase precipitates after aging at 438 K for 8 h; Q-phase is at the core and the outer wing/plate is the  $\theta'$ -phase.

	Cylindrical core (at.%)	Outer wing/plate (at.%)
Al	50.55 ± 3.36	69.35 ± 2.68
Cu	18.5 ± 3.81	27.06 ± 4.37
Mg	13.12 ± 3.17	2.08 ± 0.9
Si	16.34 ± 3.92	2.23 ± 0.74
Zn	0.88 ± 0.67	0.97 ± 0.37

electropolishing is ineffective in preparing APT specimens from W319.

Site-specific dual-beam focused-ion beam (FIB) machining was used as an alternative to electropolishing [40–46]. A number of different FIB machining methods have been developed for preparing APT specimens [47]; we utilized the technique developed for use with semiconducting materials by Thompson et al. [45]. A dual-beam FEI Helios FIB microscope, in combination with an Omniprobe micromanipulator, was used for implementing this lift-out procedure. An array of pre-fabricated Si microposts is utilized as the substrate and each micropost is the receptacle for an APT specimen [45]. We utilized an ion beam at

30 keV for all the milling and slicing steps and employed a 5 keV ion-beam energy for a clean-up step, after three stages of sharpening, to achieve a final specimen microtip diameter of 50–100 nm. This clean-up step reduces considerably the  $\text{Ga}^+$  damage in a specimen [45].

APT was performed in the laser-pulsing mode using LEAP tomography (Cameca, Madison, WI) [48–53] in the Northwestern University Center for Atom-Probe Tomography (NUCAPT). The specimen temperature was maintained at  $40 \pm 0.3$  K. The ps laser pulse energy was 0.7 nJ per pulse and the pulse repetition rate was 500 kHz. The LEAP tomographic data were analyzed employing the program IVAS 3.0 (Cameca). The  $\alpha$ -Al-matrix/Q-precipitate interfaces were delineated with one or more of the following isoconcentration surfaces: 20 Cu, 5 Mg and 6 Si at.%. The parameters used for the isoconcentration surfaces are: voxel size =  $1 \times 1 \times 1$  nm<sup>3</sup>, delocalization distance = 3 nm, sample count threshold = 1%. Efficient sampling procedures [54] were used to generate these isoconcentration surfaces and the compositional information was obtained with the proximity histogram method [55]. All the error bars presented correspond to two standard deviations for the composition analysis. Additional details concerning experimental and analysis procedures are given in Refs. [56–61].

## 2.2. Computational methods

The energetics of Zn partitioning to Q were evaluated using first-principles calculations based on the PW91 generalized gradient approximation [62] to density functional theory (DFT) [63,64], as implemented in the Vienna ab initio Simulation Package [65]. The projector augmented wave method [66,67] was used to describe the core–valence electron interaction, and tests were performed to ensure that the k-point sampling density was sufficient to converge energies to  $\sim 0.02$  eV per solute atom. A 300 eV cutoff energy was used for the plane-wave basis. Zn substitution calculations were performed using supercells of similar dimensions: a  $4 \times 4 \times 4$  supercell containing 256 atoms was used for Al, and a  $1 \times 1 \times 3$  supercell containing 96 atoms was used for Q. The shape and volume of each cell were set equal to the experimental values, and the position of each atom was optimized until the force per atom was less than  $0.02$  eV  $\text{\AA}^{-1}$ .

The Zn partitioning energy,  $E_p$ , is defined as the difference in the heats of solution ( $\Delta H$ ) for Zn in Q and for Zn in the  $\alpha$ -Al matrix:  $E_p = \Delta H(\text{Zn} \rightarrow \text{Q}) - \Delta H(\text{Zn} \rightarrow \alpha\text{-Al})$ . A negative value for  $E_p$  indicates that it is energetically preferable for Zn to partition to Q rather than to the  $\alpha$ -Al matrix; conversely, a positive value suggests that Zn solute atoms will prefer to partition to  $\alpha$ -Al. Evaluation of the partitioning energy requires that the energetics of several phases be calculated. These include: bulk  $\alpha$ -Al,  $\alpha$ -Al with Zn substitutions, bulk Q, Q with Zn substitutions, bulk Mg, bulk Si and bulk  $\theta'$  ( $\text{Al}_2\text{Cu}$ ). DFT calculations were performed on all of these phases, and the energetics were used to evaluate the partitioning energy of Zn to Q using the following expression:

$$\begin{aligned}
 E_p &= \Delta H(\text{Zn} \rightarrow \text{Q}) - \Delta H(\text{Zn} \rightarrow \alpha\text{-Al}) \\
 &= E(\text{Zn} \rightarrow \text{Q}) - \{E(\text{Q}) - \mu(\text{x}) + \mu(\text{Zn})\} \\
 &\quad - \{E(\text{Zn} \rightarrow \alpha\text{-Al}) - [E(\alpha\text{-Al}) - \mu(\text{Al}) + \mu(\text{Zn})]\} \\
 &= E(\text{Zn} \rightarrow \text{Q}) - E(\text{Q}) - E(\text{Zn} \rightarrow \alpha\text{-Al}) + E(\alpha\text{-Al}) \\
 &\quad + \mu(\text{x}) - \mu(\text{Al})
 \end{aligned} \tag{1}$$

Here  $E(\text{Zn} \rightarrow \text{Q})$  and  $E(\text{Zn} \rightarrow \alpha\text{-Al})$  are the respective energies of supercells of Q and  $\alpha\text{-Al}$ , each containing one substitutional Zn atom. Likewise,  $E(\text{Q})$  and  $E(\alpha\text{-Al})$  are the energies of pristine supercells of Q and  $\alpha\text{-Al}$  without Zn substitution.  $\mu(\text{x})$  refers to the chemical potential of the atom x in Q, which is displaced by a Zn substitutional atom:  $\text{x} = \text{Al}, \text{Cu}, \text{Mg}$  or  $\text{Si}$ , while  $\mu(\text{Al})$  is the chemical potential of an Al atom.  $\mu(\text{Al})$  is determined assuming that local equilibrium exists between Q and  $\alpha\text{-Al}$ , resulting in the equality:  $\mu(\text{Al}) = \mu(\text{Al@Q}) = \mu(\text{Al@}\alpha\text{-Al}) = E(\alpha\text{-Al})/N$ , where  $E(\alpha\text{-Al})$  is defined above and  $N$  is the number of atoms in the  $\alpha\text{-Al}$  supercell. Similarly,  $\mu(\text{Cu})$  can be determined by assuming equilibrium between Q and  $\theta'$  [68,32].

Unfortunately, it is not possible to determine uniquely the chemical potentials for the remaining components,  $\text{x} = \text{Si}$  and  $\text{Mg}$ . Their values can, however, be established to within a rather narrow energy range. To accomplish this we first note that the chemical potentials of Mg and Si in Q,  $\mu(\text{Mg@Q})$  and  $\mu(\text{Si@Q})$ , must be less than or equal to their values in their respective elemental phases:

$$\mu(\text{Mg@Q}) \leq \mu(\text{Mg@bulk Mg}), \text{ and} \tag{2a}$$

$$\mu(\text{Si@Q}) \leq \mu(\text{Si@bulk Si}) \tag{2b}$$

These inequalities establish upper limits to the chemical potentials. In the case of Si, the lower limit to  $\mu(\text{Si@Q})$  may be established by setting  $\mu(\text{Mg@Q}) = \mu(\text{Mg@bulk Mg})$  and solving:

$$\begin{aligned}
 \mu(\text{Q}) &= 3\mu(\text{Al@}\alpha\text{-Al}) + 2\mu(\text{Cu@}\theta') \\
 &\quad + 9\mu(\text{Mg@bulk Mg}) + 7\mu(\text{Si})
 \end{aligned} \tag{3}$$

for  $\mu(\text{Si})$ . An analogous procedure is used to determine  $\mu(\text{Mg})$ . Applying this approach, we find that  $\mu(\text{Si})$  lies within the range  $-5.76$  to  $-5.43$  eV, while  $\mu(\text{Mg})$  falls within  $-1.78$  to  $-1.52$  eV. As described below, the uncertainties in these chemical potentials are not large enough to alter trends in the partitioning behavior of Zn.

### 3. Results

#### 3.1. As-solutionized microstructure of W319

The alloy W319 has a multiple-phase dendritic structure in as-solutionized condition as shown in Fig. 1a and b. The microstructure typically comprises an  $\alpha\text{-Al}$  (face centered cubic) matrix containing eutectic Si, an intermetallic phase commonly known as the script phase and porosity. The stoichiometry of the script phase was reported to be  $\text{Al}_{15}(\text{Fe}, \text{Mn})_3\text{Si}_2$  [5,24]. It was, however, recently shown to be a cubic phase with the stoichiometry  $\text{Al}_{19}\text{Fe}_4\text{MnSi}_2$  [69]. The  $\theta'$ - and Q-phase precipitates do not occur in the

as-solutionized condition and appear only upon aging; moreover, these precipitates are not resolved at the length scale of Fig. 1.

#### 3.2. Thermal analyses

Fig. 2 shows the isochronal DSC plots of W319 samples in the as-solutionized condition, and after aging at three different temperatures. The solutionized sample exhibits a low-temperature endotherm (peak “a”) corresponding to the dissolution of GP zones followed by two consecutive exotherms (peaks “b” and “c”); peak “b” corresponds to the precipitation of the Q-phase and peak “c” to that of the  $\theta'$ -phase [10,70]. The last endotherm (peak “d”) signifies dissolution of all the precipitates. As anticipated, the first three peaks diminish monotonically with increasing aging temperature.

#### 3.3. X-ray analyses: Q-phase precipitates

Powder diffraction analyses performed using synchrotron radiation confirmed the presence of Q-phase precipitates in the aged W319 samples. All three aging conditions record essentially similar diffraction patterns. Fig. 3 displays a typical X-ray diffraction powder pattern of the W319 alloy aged at 463 K for 8 h. The major reflections are from the  $\alpha\text{-Al}$  matrix, Si and the script phase. Additionally, reflections from  $\theta'$  and Q-phase precipitates are identified. Peaks corresponding to the (002), (110) and (121) reflections of the Q-phase precipitates are observed at  $2\theta$  values of  $14.06^\circ$ ,  $14.28^\circ$  and  $23.75^\circ$ , respectively. No peaks corresponding to GPII zones are detected even at the lowest aging temperature, 438 K, consistent with the DSC results. Reflections from equilibrium incoherent  $\theta$ -phase precipitates are detected when aging at 533 K.

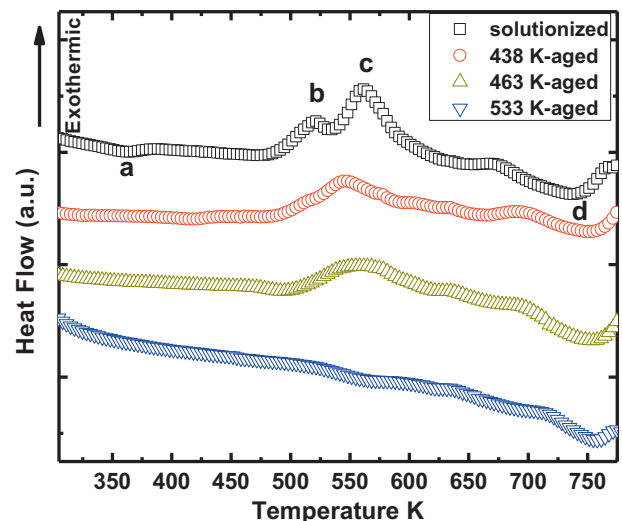


Fig. 2. DSC plots of solutionized and aged W319 samples. First endotherm “a” corresponds to the dissolution of GP zones, whereas the exotherms “b” and “c” correspond to the precipitation of the Q-phase and  $\theta'$ -precipitates, respectively. The last endotherm “d” signifies the dissolution of the precipitates.

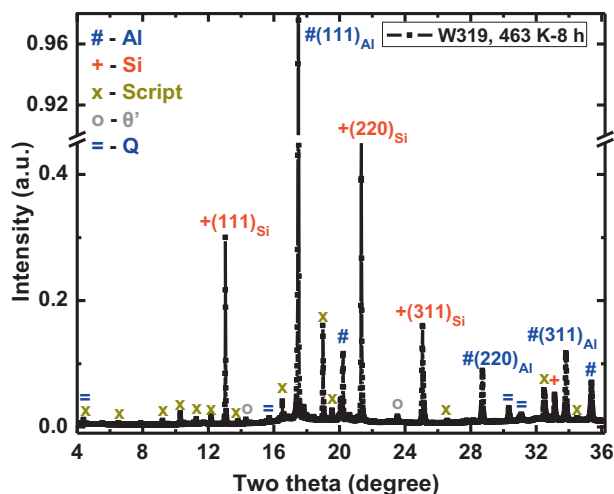


Fig. 3. Representative diffraction pattern of the aged W319 sample, obtained using synchrotron radiation at the Advanced Photon Source, Argonne National Laboratory. This is an example for a specimen aged at 463 K for 8 h.

### 3.4. TEM analyses

TEM analyses of the aged W319 samples, Fig. 4, were found to be consistent with the XRD and DSC studies. Both  $\theta'$  and Q-phase precipitates are observed in all three aging conditions, as displayed in the  $\langle 100 \rangle_{\alpha-Al}$ -zone bright-field micrographs, Fig. 4a, c and d, and the high-resolution TEM micrograph, Fig. 4b. The corresponding diffraction patterns are given in insets. The diffraction patterns display a combination of reflections from  $\alpha$ -Al along with different variants of  $\theta'$ - and Q-phase precipitates [10,34]. As expected from our DSC analysis that shows completion of dissolution of GP zones (marked “a” in Fig. 2) at 385 K, no GP zones were detected in any of these aged samples. This is also corroborated by the XRD analysis in the previous section. Q-phase precipitates exhibit needle- or rod-like morphologies with the long axis parallel to  $\langle 100 \rangle_{\alpha-Al}$ ;  $\theta'$ -precipitates are platelet-shaped with coherent  $(001)_{\theta'} \parallel \{001\}_{\alpha-Al}$  interfaces parallel to their broad faces: Fig. 4b is a high-resolution TEM micrograph of

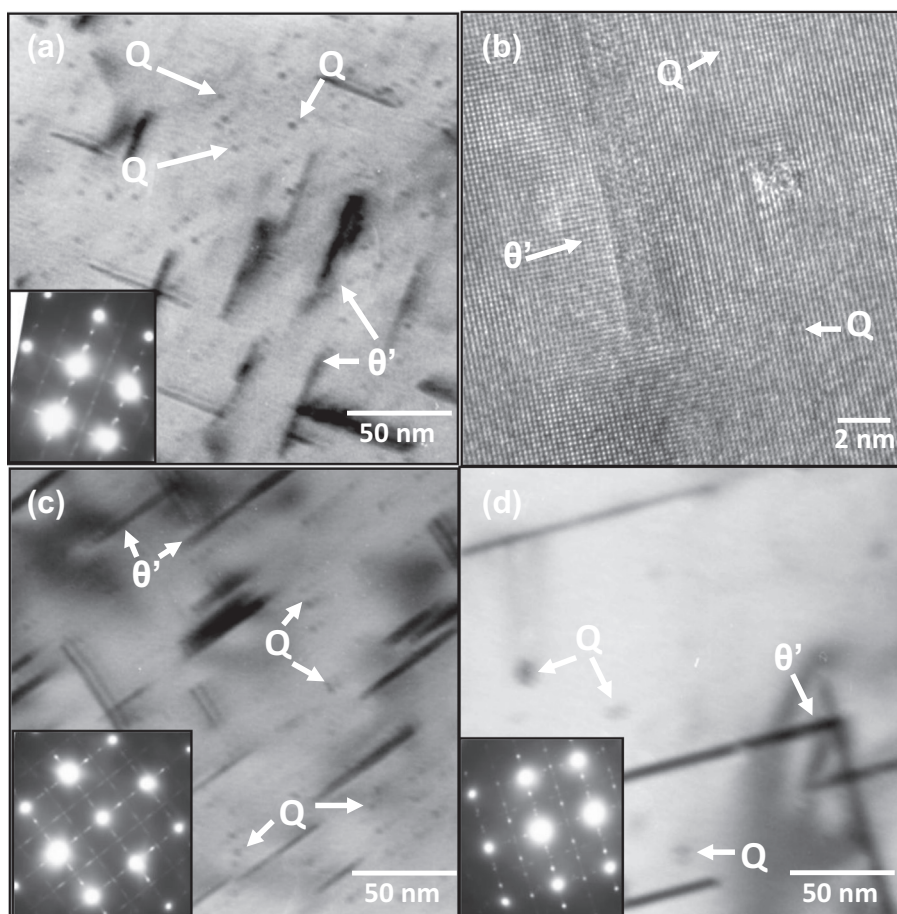


Fig. 4. Transmission electron micrographs depicting Q-phase and  $\theta'$ -precipitates for  $\langle 100 \rangle_{Al}$  zone axis: (a) and (b) are bright field and high resolution TEM images, respectively, after aging at 438 K for 8 h; (c) and (d) are bright field images after aging at 463 K for 8 h and at 533 K for 4 h, respectively. Corresponding selected area diffraction patterns are inset in the micrographs.

the  $\langle 100 \rangle_{\alpha\text{-Al}}$ -zone axis. We note, as shown in Fig. 4b, that the typical diameter of Q-phase precipitates after aging at 433 K for 8 h is  $\sim 2$  nm. With increasing aging temperature the precipitates grow in size but decrease in number density, which implies growth and coarsening.

### 3.5. APT analyses: mass spectra, microstructure and composition

All of the elements listed in Table 1 except Fe and Mn are detected in the mass spectra, Fig. 5. No Fe or Mn is detected because of their low solubility in Al [39,71] and because they form intermetallic compounds, such as the script phase, which are deliberately excluded from the region of interest (ROI). Field-evaporated Al occurs in the singly charged ( $^{27}\text{Al}^{1+}$ ) and doubly charged states ( $^{27}\text{Al}^{2+}$ ), whereas the Al hydrides ( $^{27}\text{AlH}^+$ ,  $^{27}\text{AlH}_2^+$ ) are always in the singly charged state, Fig. 5. The isotopes of Si ( $^{28}\text{Si}^{2+}$ ,  $^{29}\text{Si}^{2+}$  and  $^{30}\text{Si}^{2+}$ ) appear only in the doubly charged state, Fig. 5, and this helps for delineating the Si peak ( $^{28}\text{Si}^{2+}$ ) in the absence of the doubly charged Al-hydride peak. The isotopes of Mg ( $^{24}\text{Mg}^{2+}$ ,  $^{25}\text{Mg}^{2+}$  and  $^{26}\text{Mg}^{2+}$ ) also occur in the doubly charged state, Fig. 5. The two isotopes of Cu ( $^{63}\text{Cu}^{1+}$  and  $^{65}\text{Cu}^{1+}$ ) and their hydrides are present in the singly charged state, whereas the three most abundant isotopes of Zn ( $^{64}\text{Zn}^{2+}$ ,  $^{66}\text{Zn}^{2+}$  and  $^{68}\text{Zn}^{2+}$ ) occur in the doubly charged state in the mass spectra, Fig. 5. Thus the mass spectra confirm that all relevant elements can be successfully identified employing APT analyses.

#### 3.5.1. Aging at 438 K for 8 h

Along with  $\theta'$ -platelets, thin rod-shaped Q-phase precipitates are observed in the samples aged at 438 K for 8 h. Fig. 6a shows a typical three-dimensional (3-D) reconstruction of an analyzed volume containing  $\sim 11 \times 10^6$  atoms; only Cu (red) and Mg (green) atoms are displayed for clarity. Fig. 6b–d displays the Q-phase precipitates as delineated by Cu, Mg and Si isoconcentration surfaces, respectively. They highlight the fact that the Q-phase precipitates are rich in Cu, Mg and Si. The average dimensions of the Q-phase precipitates are:  $20.02 \pm 1.5$  nm long and  $2.1 \pm 0.1$  nm in diameter, and their number density is  $N_v = 8.1 \pm 0.1 \times 10^{22} \text{ m}^{-3}$ .

The proximity histogram (proxigram for short) method [54,55] was used to analyze the composition of Q-phase precipitates as a function of distance normal to the 9 at.% Cu isoconcentration surface, Fig. 7. The solid vertical line indicates the location of the heterophase interface between the  $\alpha\text{-Al}$  matrix and the Q-phase precipitates, which is, by definition, at the inflection point of the Al concentration profile. The spatial composition profiles of the Q-phase precipitates and the  $\alpha\text{-Al}$  matrix are displayed on the right- and left-hand sides of this line, respectively. The average chemical composition of the Q-phase precipitates is for 50 precipitates:  $44.23 \pm 5.2\text{Al}-22.56 \pm 1.74\text{Cu}-14.89 \pm 2.87\text{Mg}-17.12 \pm 1.14\text{Si}-1.08 \pm 0.44\text{Zn}$  at.%. Compared

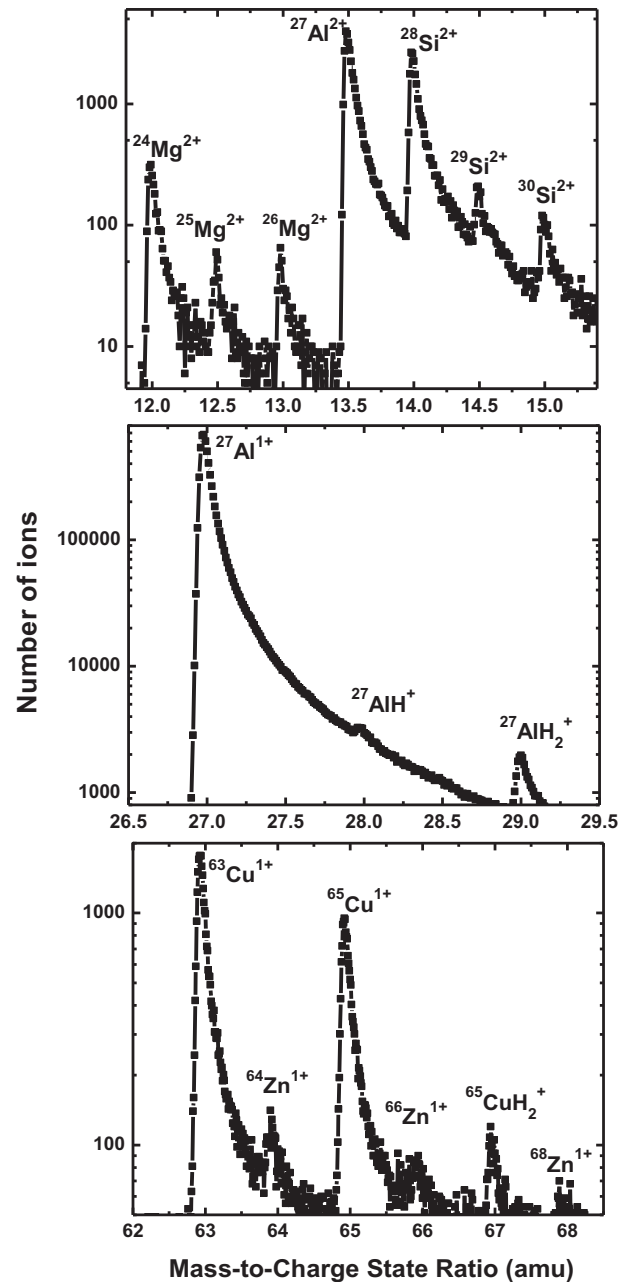


Fig. 5. Representative mass spectra obtained from a specimen of W319 that was prepared using a FEI Helios dual-beam FIB microscope. All the elements present in the alloy, except Fe and Mn, are detected in the mass spectra.

to earlier reports [8,14,15,21,23], this composition is considerably richer in Al and Cu and leaner in Mg and Si. We observe considerable partitioning of Zn to the Q-phase precipitates in these samples. No perceptible localized solute segregation is, however, detected in the vicinity of the  $\alpha\text{-Al}/\text{Q-phase}$  heterophase interface for this aging condition.

In addition to the Q-phase precipitates, the Cu-isoconcentration surface, Fig. 6b, also reveals  $\theta'$ -platelets and co-precipitation of  $\theta'$  and Q-phase precipitates, as indicated by arrows. We find that co-precipitation of  $\theta'$  and Q precipitates is present in almost every APT dataset obtained for

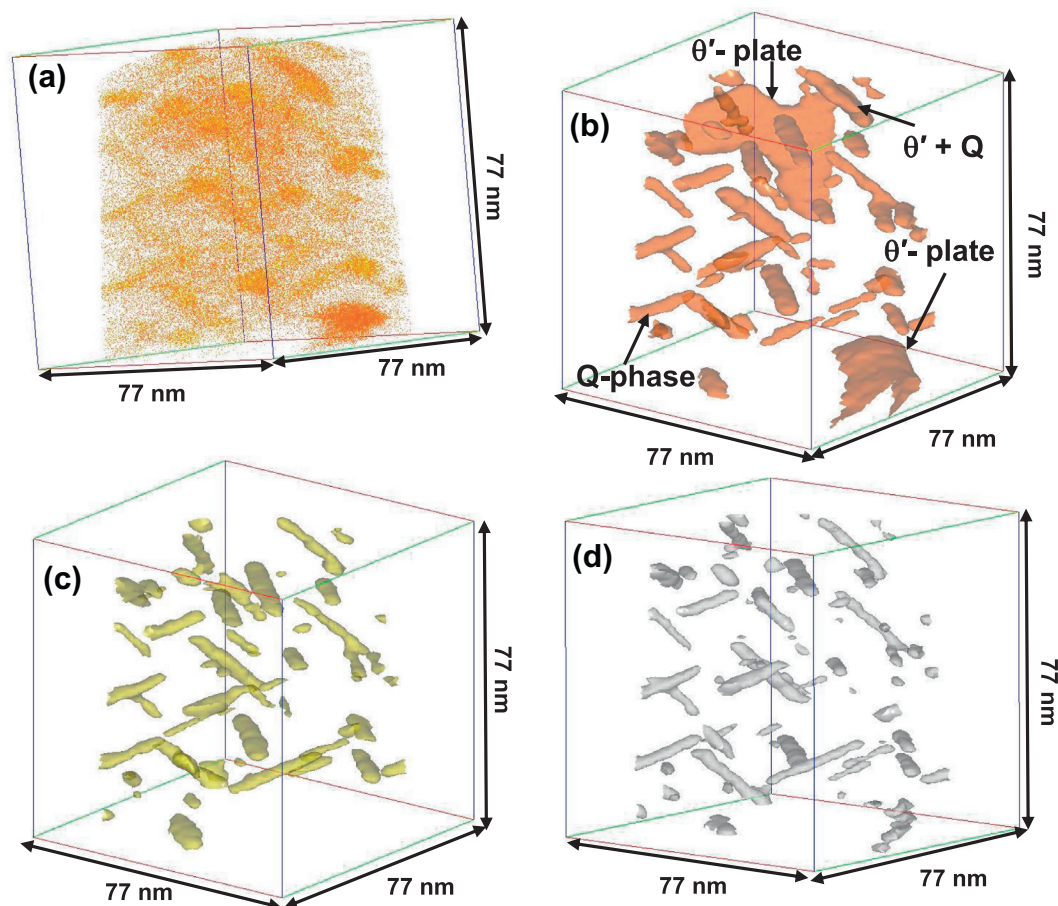


Fig. 6. (a)–(d) 3-D reconstructions of a sample of W319 aged 438 K for 8 h. Only Cu and Mg atoms are displayed in red and green, respectively in (a). Isoconcentration surfaces are created with respect to Cu, Mg and Si in (b)–(d), respectively; Cu-isoconcentration surface delineates both Q-phase and  $\theta'$ -precipitates, whereas only Q-phase precipitates are highlighted utilizing Mg and Si isoconcentration surfaces. (For interpretation of the references to color in this figure legend, the reader is referred to the web version of this article.)

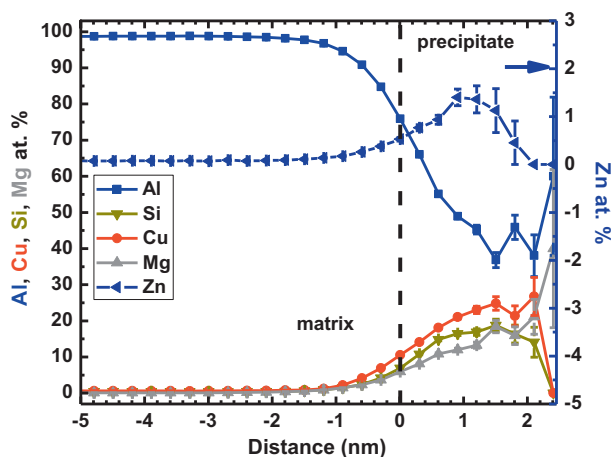


Fig. 7. Proximity histogram from a sample aged at 438 K for 8 h.

this aging condition, and occurs in slightly less than 5% of the total number of precipitates observed. Fig. 8a–c demonstrates one example of co-precipitation taken from the same dataset as in Fig. 6b. Fig. 8a displays the plate-shaped

precipitate in isolation, delineated by a Cu-isoconcentration surface. Fig. 8b displays the same precipitate with its Cu-rich outer wing/plate and a cylindrical core highlighted by a (Si + Mg)-isoconcentration surface. The cylindrical core, rich in Mg and Si, is separated for the purpose of display, Fig. 8c.

The Cu-rich outer wing/plate and the Si and Mg-rich core were analyzed separately using the proxigram method. Table 3 summarizes their respective chemical compositions. These data indicate that the Cu-rich wing/plate corresponds to the  $\theta'$ -phase with a composition that indicates significant solute partitioning:  $27.06 \pm 4.37$  Cu,  $2.084 \pm 0.9$  Mg,  $2.23 \pm 0.74$  Si and  $0.97 \pm 0.37$  Zn at.%. (Recall that  $\theta'$  has the stoichiometry  $\text{Al}_2\text{Cu}$ .) Prior experiments and modeling have also revealed significant partitioning of Si and Mg to  $\theta'$ -precipitates [32,33]. Alternatively, the composition of the core precipitate, Fig. 8c, is consistent with that of the Q-phase and hence rich in Mg and Si:  $13.12 \pm 3.17$  Mg and  $16.34 \pm 3.92$  Si at.%. This co-precipitated Q-phase has, however, less Cu than the isolated Q-phase precipitates, Fig. 6b–d, for this aging condition.

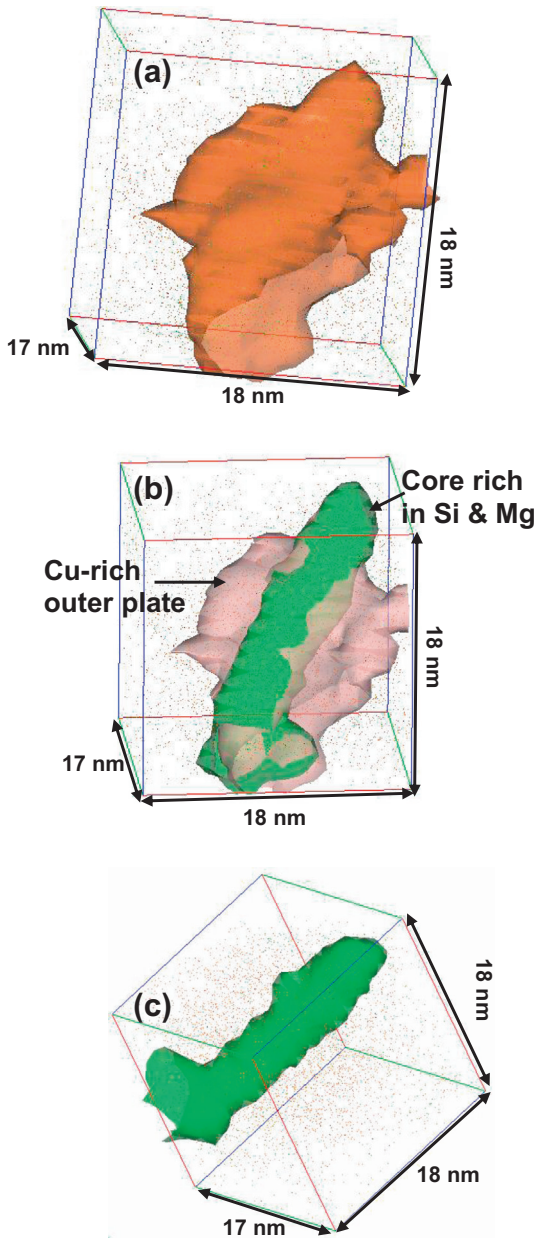


Fig. 8. Co-precipitation of Q-phase and  $\theta'$ -precipitates in W319 after aging at 438 K for 8 h: (a) Cu isoconcentration surfaces do not differentiate between the precipitates; (b) isoconcentration surface created with respect to Si plus Mg successfully delineates Q-phase core from the Cu-rich  $\theta'$ -phase present at the outer plate; and (c) Q-phase core rich in Si and Mg is isolated. Co-precipitation is observed for the three aging conditions.

### 3.5.2. Aging at 463 K for 8 h

Aging for 8 h at 463 K (T6 treatment) gives rise to thin rod-shaped Q-phase precipitates that are similar to what is observed when aging at 438 K. This behavior is illustrated in the 3-D reconstructions in Fig. 9a and b, which contain  $\sim 16 \times 10^6$  atoms. Fig. 9a displays the presence of  $\theta'$ -platelets and Q-phase precipitates, indicated by arrows; for clarity, only Cu (red) and Mg (green) atoms are displayed. Cu-rich (red atoms)  $\theta'$ -platelets exhibit a distinctly different morphology compared to the Q-phase precipitates, which are much richer in Mg (green atoms).

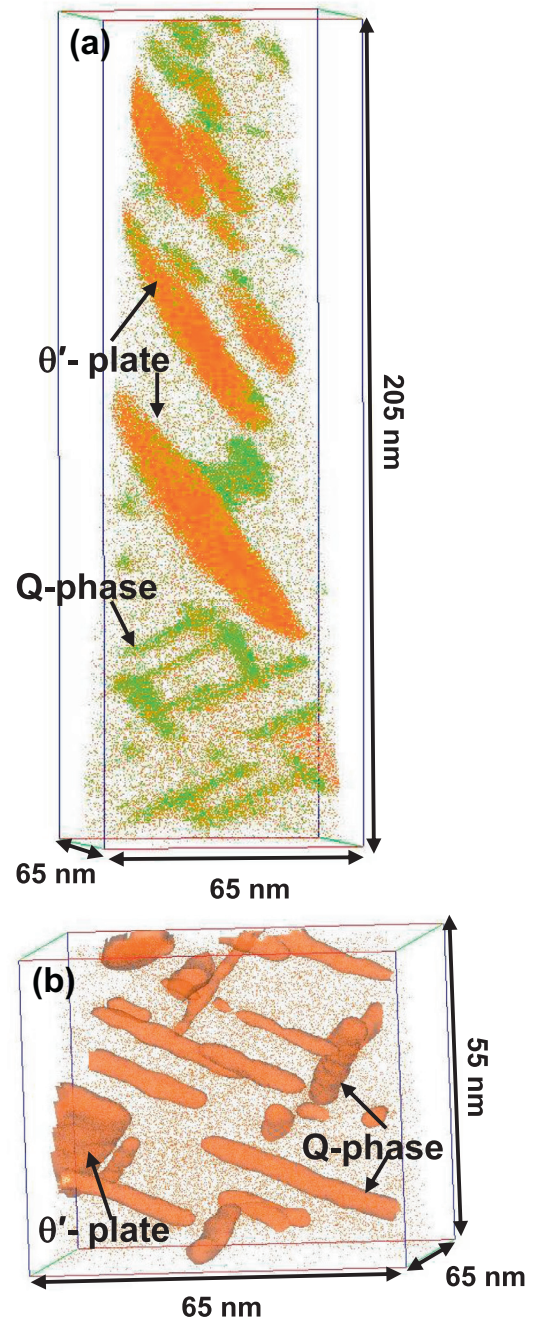


Fig. 9. 3-D reconstructions of a sample of W319 aged 463 K for 8 h: (a) only Cu (red) and Mg (green) atoms are displayed in the atom map. Mg-rich Q-phase and Cu-rich  $\theta'$ -precipitates are distinctly visible; and (b) Cu-isoconcentration surface delineates both Q-phase and  $\theta'$ -precipitates. (For interpretation of the references to color in this figure legend, the reader is referred to the web version of this article.)

Q-phase precipitates from the same dataset are highlighted using a 9 at.% Cu isoconcentration surface, Fig. 9b. The average length of the Q-phase precipitates is  $25.01 \pm 1.47$  nm, which is  $\sim 25\%$  longer than for the 438 K aging condition, while their typical diameter is essentially unchanged at  $2.03 \pm 0.27$  nm. Additionally, the number density of the Q-phase precipitates is decreased by half

to  $5.01 \pm 0.2 \times 10^{22} \text{ m}^{-3}$ , when compared to aging at 438 K.

Compositional analyses of the Q-phase precipitates using the proxigram methodology [54,55] are displayed in Fig. 10. The average chemical composition of these precipitates does not significantly differ from what we observed when aging at 438 K. While there is essentially no change in the Cu concentration, the concentration of Mg increases slightly to  $17.4 \pm 1.9 \text{ at.}\%$ , whereas Si decreases to  $15.8 \pm 1.45 \text{ at.}\%$ . Furthermore, there is a  $\sim 25\%$  reduction in the extent of Zn partitioning for this aging condition when compared to aging at 438 K. Once again, no evidence of localized solute segregation at the  $\alpha\text{-Al}/\text{Q-phase}$  heterophase interface is detected. Co-precipitation of the  $\theta'$ - and the Q-phase precipitates is, however, observed for this aging condition as well.

### 3.5.3. Aging at 533 K for 4 h

The Q-phase precipitates observed in samples aged at 533 K for 4 h (T7 treatment) are considerably larger and wider than those found in either the 438 or 463 K treatments. Their number density is smaller by an order of magnitude,  $N_v = 5.37 \pm 0.4 \times 10^{21} \text{ m}^{-3}$ , and therefore they become more difficult to locate within an analysis volume. Fig. 11a displays a typical 3-D reconstruction of an analyzed volume for this aging condition containing both  $\theta'$ -platelets and Q-phase precipitates, indicated by arrows; Al and Cu atoms are displayed in blue and red, respectively, and Q-phase precipitates are delineated by Mg-isoconcentration surface. This dataset contains  $\sim 12 \times 10^6$  atoms. Fig. 11b displays one isolated Q-phase precipitate from the same dataset. Examples of co-precipitation of the  $\theta'$ - and the Q-phase precipitates are also found for this aging condition, but at a relatively lower frequency.

Composition analyses of the Q-phase precipitates were performed with the proxigram displayed in Fig. 12. As compared to the other two aging conditions, Q-phase precipitates formed upon aging at 533 K exhibit a significant increase in the concentrations of Mg and Si along with a

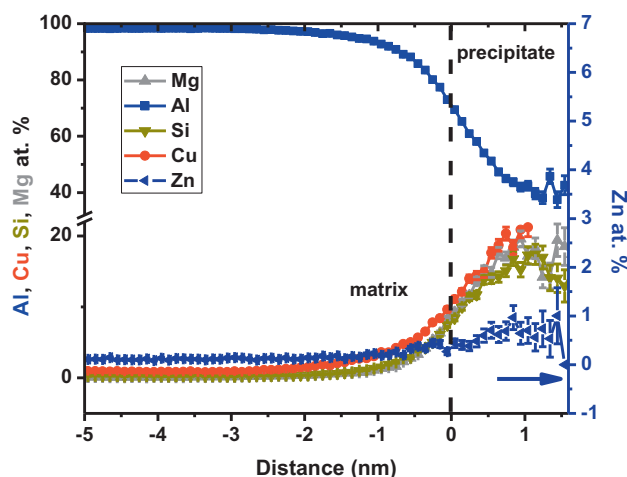


Fig. 10. Proximity histogram from a sample aged at 463 K for 8 h.

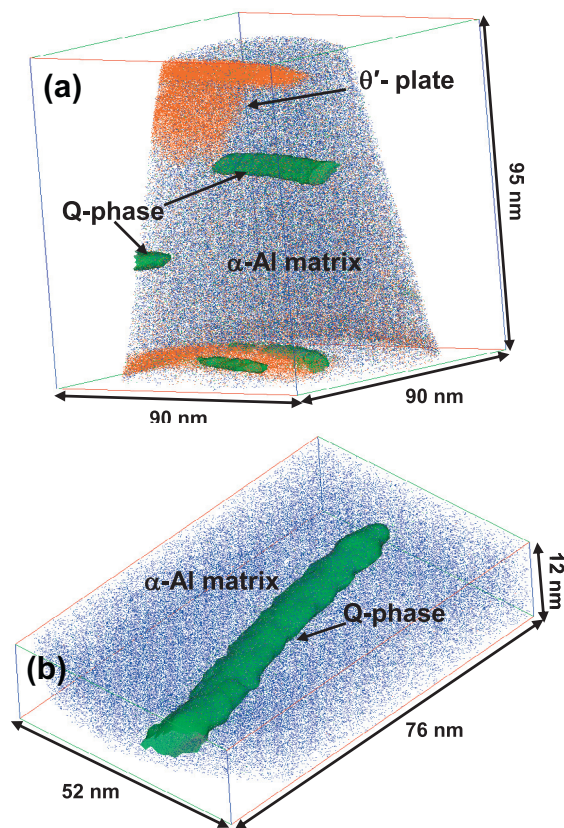


Fig. 11. 3-D reconstructions of a sample of W319 aged at 533 K for 4 h. Al (blue) and Cu (red) and Mg (green) atoms are displayed in the atom map: (a) Mg-isoconcentration surface delineates the Q-phase precipitates and Cu-rich  $\theta'$ -precipitates are also visible; and (b) a large rod-shaped Q-phase precipitate is isolated. (For interpretation of the references to color in this figure legend, the reader is referred to the web version of this article.)

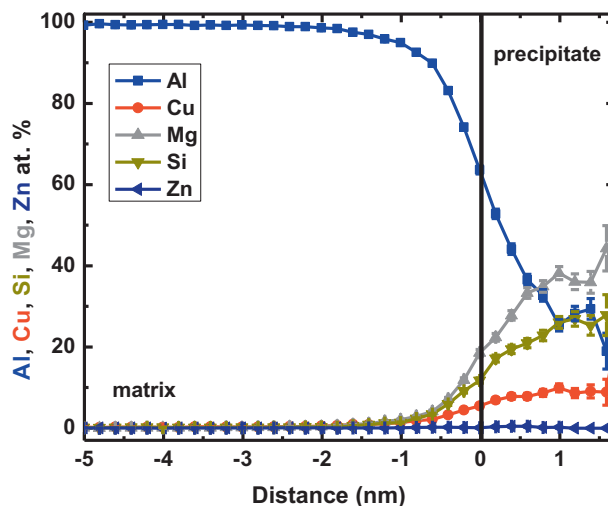


Fig. 12. Proxigram from a sample aged at 533 K for 4 h.

large reduction in Cu concentration. The concentrations of Mg, Si and Cu are  $36.84 \pm 2.08$ ,  $26.17 \pm 1.89$  and  $9.23 \pm 1.24 \text{ at.}\%$ , respectively. Table 4 compares the chemical compositions of the Q-phase precipitates measured

after aging for 4 h at 533 K with that of the two other aging treatments. Concomitantly, there is an order-of-magnitude reduction in the Zn concentration in the Q-phase precipitates upon aging at 533 K as compared to 463 K aging, which decreases from  $0.73 \pm 0.15$  to  $0.074 \pm 0.05$  at.% Zn. Similar to the other aging conditions, the analysis does not reveal any localized solute segregation at the  $\alpha$ -Al/Q-phase interface.

### 3.6. First-principles calculations

First-principles calculations were used to assess the energetics of Zn solute partitioning to the Q-phase from the  $\alpha$ -Al matrix. Fig. 13 depicts the conventional unit cell of the Q-phase; we adopt the crystal structure and  $\text{Al}_3\text{Cu}_2\text{Mg}_9\text{Si}_7$  (14.3Al–9.5Cu–42.9Mg–33.3Si at.%) stoichiometry proposed by Wolverton [15] based on first-principles calculations on the partial structure suggested by Arnberg and Aurivillius [14].<sup>1</sup> A total of nine distinct sites in Q are available for Zn substitution: one Al site, two Cu sites, three Mg sites and three Si sites; these sites are identified in Fig. 13. Separate Zn substitution calculations were performed for each site.

Fig. 14 summarizes the calculated partitioning energy  $E_p$  of Zn solutes to the Q-phase for each of the nine distinct substitutional sites. The partitioning energies are relative to Zn substitution in  $\alpha$ -Al and we adopt a sign convention where a positive partitioning energy indicates that Zn partitioning to the Q-phase is energetically unfavorable, that is, endothermic. As can be seen in Fig. 14, all of the partitioning energies are relatively large and positive regardless of the substitutional site, with values ranging from 0.32 to 1.13 eV per Zn atom. In the case of Mg and Si, the uncertainty in the chemical potential (described above) is too small to alter the qualitative behavior in partitioning energetics: any value within the range of possible chemical potentials for these elements results in endothermic partitioning energies.

Taken together, the partitioning energies indicate that there is no thermodynamic driving force for Zn to partition to the Q-phase. Prior experiments and calculations have also found limited evidence for Zn segregation at heterophase interfaces between  $\alpha$ -Al and the  $\theta'$ -phase precipitates [33]. Rather, the energetics of Zn substitution favor partitioning of Zn to  $\alpha$ -Al or potentially to the  $\theta'$ -phase. In summary, the energetics of Zn partitioning indicate that there is no thermodynamic driving force underlying the presence of Zn in Q-phase precipitates. We therefore speculate that the presence of Zn may be explained by kinetic effects: Zn may

Table 4

Compositional evolution of the Q-phase precipitates with aging temperatures.

	438 K–8 h (at.%)	463 K–8 h (at.%)	533 K–4 h (at.%)
Al	44.23 $\pm$ 5.2	44.07 $\pm$ 4.3	27.74 $\pm$ 1.94
Cu	22.56 $\pm$ 1.74	22.0 $\pm$ 3.2	9.23 $\pm$ 1.24
Mg	14.89 $\pm$ 2.87	17.4 $\pm$ 1.9	36.84 $\pm$ 2.08
Si	17.12 $\pm$ 1.14	15.8 $\pm$ 1.45	26.17 $\pm$ 1.89
Zn	1.08 $\pm$ 0.44	0.73 $\pm$ 0.15	0.074 $\pm$ 0.05

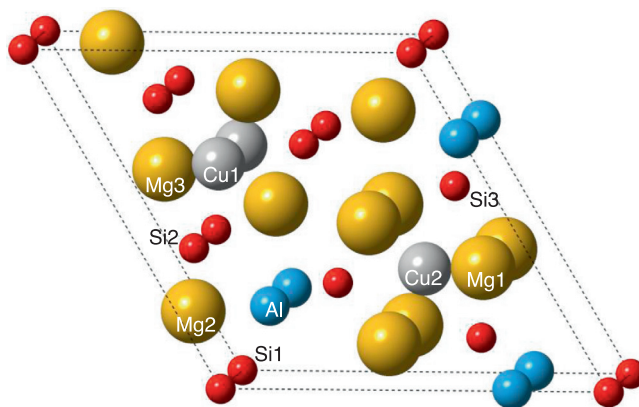


Fig. 13. Conventional unit cell for the Q-phase,  $\text{Al}_3\text{Cu}_2\text{Mg}_9\text{Si}_7$ . Al atoms are blue, Cu is grey, Mg is orange and Si is red. Labels identify the nine symmetry-distinct sites examined for Zn substitution. (For interpretation of the references to color in this figure legend, the reader is referred to the web version of this article.)

play a role in precipitate nucleation and remain trapped within the precipitate due to slow diffusion.

## 4. Discussion

We present an APT analysis of Q-phase precipitates in the high-Si commercial Al-alloy W319. Contrary to what is commonly acknowledged, our compositional analyses reveal (Table 4) that these precipitates first emerge as a Cu-rich phase after aging at 438 K for 8 h with a ratio between the concentrations of Mg and Si ( $[\text{Mg}]/[\text{Si}]$ ) of 0.87. This ratio increases to a value of 1.10 after aging at 463 K for 8 h, even though the concentration of Cu remains virtually unchanged. Further changes to the  $[\text{Mg}]/[\text{Si}]$  ratio are observed upon aging at 533 K for 4 h –  $[\text{Mg}]/[\text{Si}] = 1.41$ . Simultaneously, the Cu concentration undergoes a  $\sim 60\%$  reduction to  $9.23 \pm 1.24$  at.%. Aging at 533 K for 4 h therefore results in Q-phase precipitates that are rich in Mg and Si and lean in Cu, with an overall composition of 28Al–9Cu–37Mg–26Si at.%.

In Table 5 we compare the compositional evolution of Q-phase precipitates as measured in the current study with archival literature results. Our measured composition after aging at 533 K, Table 4, is similar to those of Phragmen [22] and Cayron et al. [26]. The study by Cayron et al. [26] identified two possible structural precursors to the Q-phase precipitates, QC and QP in a T6-tempered

<sup>1</sup> While the stoichiometry of the adopted structure differs somewhat from our measured values, to our knowledge Wolverton's model [15] is the only available complete crystal structure for the Q-phase. Moreover, given the trends in the calculated partitioning energies described below, all of which indicate that Zn partitioning to Q is highly endothermic, we do not anticipate that other stoichiometries will alter our conclusions.

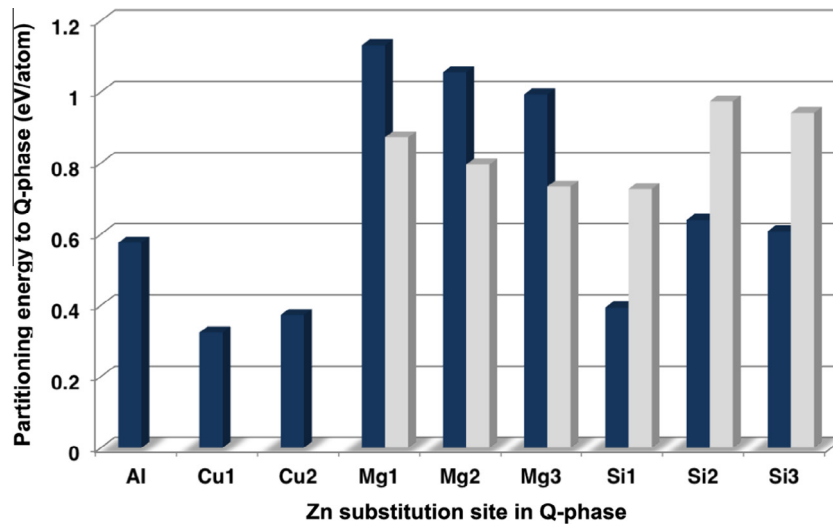


Fig. 14. Partitioning energies of Zn atoms to the Q-phase as a function of the Zn substitution site. The partitioning energy is relative to the heat of solution for Zn in  $\alpha$ -Al; a positive partitioning energy indicates that Zn substitution to Q is energetically unfavorable compared to Zn substitution in  $\alpha$ -Al. Two partitioning energies (blue bars and grey bars) are given in the case of substitution on Mg and Si sites. These represent the range of possible values of the Mg and Si chemical potentials (see text for further information). (For interpretation of the references to color in this figure legend, the reader is referred to the web version of this article.)

Table 5  
Chemical composition of the Q-phase as reported in the literature.

	$\text{Al}_5\text{Cu}_2\text{Mg}_8\text{Si}_6$ (PhragmenG.)	$\text{Al}_4\text{Cu}_2\text{Mg}_8\text{Si}_7$ (Arnberg et al.)	$\text{Al}_5\text{Cu}_2\text{Mg}_8\text{Si}_6$ (Cayron et al.)	$\text{Al}_4\text{Cu}_1\text{Mg}_6\text{Si}_6$ (Matsuda et al.)	$\text{Al}_3\text{Cu}_2\text{Mg}_9\text{Si}_7$ (Wolverton C.)
Al	23.8	19.04	23.8	23.5	14.28
Cu	9.52	9.52	9.52	5.9	9.52
Mg	38.09	38.09	38.09	35.3	42.85
Si	28.57	33.33	28.57	35.3	33.33

SiC-reinforced Al–Cu–Mg–Ag alloy. Based on EDS analyses, these precursors were reported as having compositions that were rich in Mg and Si and lean in Cu. In contrast, our data show that the Q-phase particles formed following the low temperature aging treatments (438 and 463 K) are rich in Cu and lean in Mg and Si. Another study based on EDS analyses by Matsuda et al. [27] reported much lower concentrations of Cu and higher concentrations of Si, Table 5. Furthermore, first-principles calculations by Wolverton [15] identified  $\text{Al}_3\text{Cu}_2\text{Mg}_9\text{Si}_7$  (14.3Al–9.5Cu–42.9Mg–33.3Si at.%) as the most stable stoichiometric composition for the Q-phase. That stoichiometry – which contains higher concentrations of Mg and Si at the expense of Al – does not, however, agree with the present experimental results.

Three prior studies reported compositions of Q-phase precipitates in Al alloys [26,27,34]. As those studies exhibited bulk and Q-phase compositions that in some cases differ from the present study, it is worthwhile to consider whether a relationship exists between the composition of the Q-phase precipitates and that of the matrix within which the precipitates form. The concentrations of the three main solutes used in the previous reports are compared with the present study in Table 6. Despite the higher Mg and lower Si matrix concentrations in Ref. [26], the

Table 6  
Comparison of concentrations of Si, Cu and Mg in the alloys studied in the current study and Refs. [26,27,34].

	Weight%		
	Si	Cu	Mg
Present study	7.48	3.53	0.31
Cayron et al. [26]	1.2	4	1
Matsuda et al. [27]	0.37	0.5	0.63
Hwang et al. [34]	6.7	3.75	0.45

composition of Q-phase precipitates reported in Ref. [26] is very similar to that observed in the present study after aging at 533 K. On the other hand, the matrix of Ref. [27] is richer in Mg and leaner in Si, yet the precipitates in Ref. [27] exhibit lower Mg and higher Si concentrations than in our analysis. Finally, we note that the precipitate composition in Ref. [34] differs from the current study, yet the bulk compositions are very similar. These comparisons suggest that variations in matrix composition (at least at the levels considered here) do not yield a clear trend in the composition of Q-phase precipitates.

A further observation relates to the presence of other solutes in the Q-phase: to our knowledge, all prior studies of this phase have not considered this possibility. Our analyses

provide the first definitive experimental evidence of partitioning of Zn to the Q-phase precipitates for all the three aging conditions. The Zn concentration is the highest at  $1.08 \pm 0.44$  at.% after aging at 438 K and it declines to  $\sim 750$  at. ppm for an aging treatment at 533 K. Our first-principles calculations of the Zn partitioning energies indicate that there is no thermodynamic driving force for Zn partitioning to the Q-phase. Rather, the energetics of Zn substitution favor partitioning of Zn to either  $\alpha$ -Al or to the  $\theta'$ -phase. Therefore, the presence of Zn in Q-phase precipitates appears to be a non-equilibrium effect, possibly related to slow diffusion of Zn out of the Q-phase. In addition to solute partitioning, Matsuda et al. [28] observed localized segregation of Cu at the  $\alpha$ -Al/Q-phase heterophase interface in an Al–Mg–Si–Cu alloy. In the current study we do not, however, find evidence for localized heterophase interfacial solute segregation in W319; rather, the shape of the concentration profiles (Figs. 7, 10 and 12) is suggestive of delocalized behavior [33].

Regarding the sequence of precipitation and precipitate morphology, the present study finds rod-shaped Q-phase precipitates,  $\theta'$ -platelets and co-precipitation of the  $\theta'$ - and Q-phase precipitates for all three aging treatments. DSC analyses, powder diffraction experiments and TEM results further clarify the identity of the precipitates, Figs. 2–4. Our DSC analyses suggest the following precipitation sequence in W319 for the aging conditions examined: GP zones  $\rightarrow$  Q  $\rightarrow$  Q +  $\theta'$ . Although there are no reports of thermal analysis of this alloy, Dutta et al. [10] and Miao and Laughlin [70] observed a similar precipitation sequence in 2014 Al-matrix composites and alloy 6022, respectively. (Alloy 6022 reportedly showed an additional  $\beta''$ -precipitate in the decomposition pathway [70].) These prior studies agree well with the fact that in all the cases of co-precipitation of Q +  $\theta'$  observed in this study, it is the Q-phase that is always at the core, Fig. 8. This suggests that the Q-phase may catalyze the heterogeneous nucleation of the  $\theta'$ -phase. Because  $\theta'$ -precipitates are known to nucleate in the strain fields of dislocations [72] and of pre-existing  $\theta'$  platelets, there exists the possibility of nucleation in the strain field of Q-phase precipitates as well. To the best of our knowledge, co-precipitation in W319 has not been reported. Weakley-Bolin et al. [5] observed Q-phase precipitates and  $\theta'$ -platelets on aging W319 at 463 and 533 K, respectively, but co-precipitation was not observed [5]. Microstructural evidence of similar co-precipitation was presented by Cayron et al. [26] in their study of a SiC-reinforced Al–Cu–Mg–Ag alloy. They used high-resolution electron microscopy and observed co-precipitation of  $\theta'$ -, Q- and QC-phases, where the QC-phase was one of two precursors of the Q-phase precipitate.

GP zones are only detected in the as-solutionized state, Fig. 2, and cease to exist after the subsequent aging treatments. XRD, Fig. 3, and TEM, Fig. 4, analyses confirm this result; this observation is consistent with prior studies [10,70]. The absence of GPII in W319 at the lowest aging temperature of 438 K suggests, however, the presence of

accelerated precipitation kinetics as compared to a binary Al–Cu alloy with a similar Cu concentration [32]. For example, prior XRD studies of aging of a binary Al–4 wt.% Cu alloy at this aging temperature by Hardy [73,74] and Silcock et al. [75] reported a majority GPII phase. At an aging temperature of 438 K, Silcock et al. [75] detected  $\sim 20$  vol.%  $\theta'$ -platelets in an Al–4 wt.% Cu alloy only when the duration of aging was  $\geq 3.5$  days. Similarly, Boyd and Nicholson [76] observed that GPII zones in a similar binary alloy commenced transforming to  $\theta'$ -platelets only when the aging time at 438 K was  $> 48$  h. In contrast, we find that  $\theta'$ -platelets with Q-phase precipitates form in W319 when aging for 8 h at 438 K.

## 5. Conclusions

The primary findings of our study can be summarized as follows:

- (1) Temporal evolution of the composition of the Q-phase precipitates in an age-hardenable high-Si commercial alloy W319 was studied utilizing correlatively the following techniques: APT, DSC, X-ray diffraction, TEM and first-principles modeling.
- (2) The very high Si concentration, 7.38 at.%, of W319 complicates the preparation of samples for APT analysis. Site-specific FIB machining was, however, utilized successfully for sample preparation and yielded reliable APT datasets.
- (3) Precipitate morphology: thin rod-shaped Q-phase precipitates ( $20.02 \pm 1.5$  nm long and  $2.1 \pm 0.1$  nm in diameter) are obtained upon aging at 438 K with a number density of  $8.1 \pm 0.1 \times 10^{22} \text{ m}^{-3}$ . Higher aging temperatures result in larger precipitates with smaller number densities:  $5.01 \pm 0.2 \times 10^{22} \text{ m}^{-3}$  at 463 K, and  $5.37 \pm 0.4 \times 10^{21} \text{ m}^{-3}$  at 533 K.
- (4) Composition evolution: aging at the lower temperatures (438 and 463 K) yields Q-phase precipitates that are rich in Cu and deficient in Mg and Si, with an overall composition of approximately 44Al–22Cu–16Mg–16.5Si at.%. The composition becomes Mg-rich after aging at 533 K for 4 h:  $\sim 28\text{Al}–9\text{Cu}–37\text{Mg}–26\text{Si}$  at.%.
- (5) Zn partitioning: APT provides evidence for partitioning of Zn to the Q-phase precipitates in W319. The Zn concentration decreases with increasing temperature from  $1.08 \pm 0.44$  at.% after aging at 438 K, to  $\sim 750$  at. ppm after aging at 533 K. First-principles calculations of the Zn partitioning energy demonstrates that Zn incorporation in the Q-phase is energetically unfavorable. Therefore, the experimental observation of Zn solutes in the Q-phase precipitates is most likely a kinetic effect arising from slow Zn diffusion and/or nucleation effects.
- (6) Precipitation sequence: DSC analyses reveal that Q-phase precipitates appear before  $\theta'$  upon aging, and the precipitation sequence in W319 is as follows: GP zones  $\rightarrow$  Q  $\rightarrow$  Q +  $\theta'$ .

- (7) Co-precipitation: co-precipitation of  $\theta'$ - and Q-phase precipitates occurs for all aging conditions in W319. The presence of co-precipitation and the sequence of precipitation suggest that existing Q-phase precipitates can act as nucleation sites for  $\theta'$ -platelets, i.e. piggy-back nucleation.
- (8) Interfacial segregation: in contrast to earlier reports, no evidence for localized solute segregation at the heterophase interface between the  $\alpha$ -Al matrix and the Q-phase precipitates was found.

## Acknowledgements

Funding for this research was provided by the Ford-Boeing-Northwestern Alliance. APT measurements were performed at the Northwestern University Center for Atom-Probe Tomography (NUCAPT). Funding for the purchase of the LEAP tomograph and for upgrades was generously provided by NSF-MRI (DMR 0420532), ONR-DURIP (N00014-0400798) and ONR-DURIP (N00014-0610539). We gratefully acknowledge the Initiative for Sustainability and Energy at Northwestern (ISEN) for grants to upgrade the capabilities of NUCAPT. The FEI dual-beam FIB is part of the EPIC facility at Northwestern, which is supported by NSF-NSEC, NSF-MRSEC, Keck Foundation, State of Illinois and Northwestern University. The authors would like to thank Sudip Kumar Sarkar and Dr. R. Tewari, BARC; Roger Alvis, Cameca; and Dr. Daniel Schreiber, Northwestern, for their kind help. We also thank Drs. Donald S. Shih and Krishnan K. Sankaran (Boeing), Prof. John Allison (formerly Ford Research Laboratory and currently University of Michigan at Ann Arbor) and Prof. Chris Wolverton (Northwestern University) for their continuous interest.

## Appendix A

### A.1. Homogenization of W319

The following equation is used to estimate the time ( $t_{0.05}$ ) to reduce a composition fluctuation for a given solute to 5% of its initial value [77]:

$$t_{0.05} \cong 0.3 \frac{\lambda^2}{D_s} \quad (\text{A.1})$$

where  $\lambda$  is the secondary dendrite arm spacing, which has a typical value of 20  $\mu\text{m}$  for alloy W319 [5], and  $D_s$  is the

Table A1  
Estimate of the homogenization times  $t_{0.05}$  for the four major solute elements in the W319 alloy.

	Diffusivity ( $\text{m}^2 \text{s}^{-1}$ )	$t_{0.05}$ (h)	Refs.
Cu	$1.54 \times 10^{-15}$ at 673 K	21.65	[78]
Mg	$1.61 \times 10^{-14}$ at 673 K	02.07	[79]
Si	$0.64 \times 10^{-13}$ at 753 K	00.52	[80]
Zn	$1.05 \times 10^{-14}$ at 673 K	03.18	[78]

diffusivity of a given solute species in aluminum at the temperatures specified in Table A1. We have calculated  $t_{0.05}$  for the four major elements in this alloy, Table A1. The analyses demonstrate that a solutionizing heat treatment for 24 h at 758 K is sufficient to achieve satisfactory homogenization, as the  $t_{0.05}$  values are less than 24 h for each solute.

## References

- [1] Kaufman JG. Introduction to aluminum alloys and tempers. Materials Park, OH: ASM International; 2000. p. 258.
- [2] Polmear IJ. Light alloys: from traditional alloys to nanocrystals. London: Elsevier Butterworth-Heinemann; 2006.
- [3] Apelian D. Worldwide report, aluminum cast alloys: enabling tools for improved performance. Wheeling, IL: NADCA; 2009.
- [4] Aaronson HI, Laird C. Ford Motor Co., Scientific Laboratory Report No. SL 67–52; 1967.
- [5] Weakley-Bolin SC, Donlon W, Wolverton C, Jones JW, Allison JE. Metall Mater Trans A 2004;35A:2407.
- [6] Chakrabarti DJ, Cheong B, Laughlin DE. In: Das SK, editor. Automotive alloys II. Pittsburgh, PA: TMS; 1998. p. 27–44.
- [7] Perovic A, Perovic DD, Weatherly GC, Lloyd DJ. Scr Mater 1999;41:703.
- [8] Weatherly GC, Perovic A, Mukhopadhyay NK, Lloyd DJ, Perovic DD. Metall Mater Trans A 2001;32A:213.
- [9] Crowther J. J Inst Metals 1949–1950;76:201.
- [10] Dutta I, Harper CP, Dutta G. Metall Mater Trans A 1994;25A:1591.
- [11] Starink MJ, Abeels VMF, van Mourik P. Mater Sci Eng A 1993;163:115.
- [12] Bronsveld PM, Starink MJ, Verwerf M, de Hosson JThM, van Mourik P. Scr Metall Mater 1995;33:427.
- [13] Dix EH, Sager GF, Sager BP. Trans AIME 1932;99:119.
- [14] Arnberg L, Aurivillius B. Acta Chem Scand A 1980;34:1.
- [15] Wolverton C. Acta Mater 2001;49:3129.
- [16] Chakrabarti DJ, Laughlin DE. Prog Mater Sci 2004;49:389.
- [17] Sagalowicz L, Lapasset G, Hug G. Philos Mag Lett 1996;74:57.
- [18] Cayron C, Buffat PA. Acta Mater 2000;48:2639.
- [19] Eskin DG. J Mater Sci 2003;38:279.
- [20] Philips HWL. Equilibrium diagrams of aluminium alloy systems. London: The Aluminum Development Association; 1961. pp. 128–33.
- [21] Cayron C, Buffat PA, Belfort O, Long S. J Mater Sci 1999;34:905.
- [22] Phragmen G. J Inst Metals 1950;77:489.
- [23] Mondolfo LF. Metallography of aluminum alloys. New York: Wiley; 1943. p. 249.
- [24] Mondolfo LF. Aluminum alloys, structure and properties. London: Butterworths; 1976. p. 564.
- [25] Gupta AK, Jena AK, Chaturvedi MC. Mater Sci Tech 1987;3:1012.
- [26] Cayron C, Sagalowicz L, Belfort O, Buffat P. Philos Mag A 1999;79:2833.
- [27] Matsuda K, Uetani Y, Sato T, Ikeno S. Metall Mater Trans A 2001;32:1293.
- [28] Matsuda K, Teguri D, Uetani Y, Sato T, Ikeno S. Scr Mater 2002;47:833.
- [29] Edwards GA, Stiller K, Dunlop GL. Appl Surf Sci 1994;76–77:219.
- [30] Edwards GA, Stiller K, Dunlop GL, Couper MJ. Acta Mater 1998;46:3893.
- [31] Murayama M, Hono K, Saga M, Kikuchi M. Mater Sci Eng A 1998;250:127.
- [32] Biswas A, Siegel DJ, Wolverton C, Seidman DN. Acta Mater 2011;59:6187.
- [33] Biswas A, Siegel DJ, Seidman DN. Phys Rev Lett 2010;105:076102-1.
- [34] Hwang JY, Banerjee R, Doty HW, Kaufman MJ. Acta Mater 2009;57:1308.
- [35] Boileau JM, Allison JE. Metall Mater Trans A 2003;34A:1807.
- [36] Delasi R, Adler PN. Metall Mater Trans A 1977;8A:1177.

- [37] Krakauer BW, Hu JG, Kuo S-M, Mallick RL, Seki A, Seidman DN, et al. *Rev Sci Instrum* 1990;61:3390.
- [38] Krakauer BW, Seidman DN. *Rev Sci Instrum* 1992;63:4071.
- [39] Massalski TB. *Binary alloy phase diagrams*. 2nd ed, 2nd ed., vol. 1. Warrendale, PA: ASM International; 1990.
- [40] Giannuzzi LA, Stevie FA. *Introduction to focused ion beams*. New York: Kluwer/Academic Press; 2004.
- [41] Giannuzzi LA, Anzalone PA, Young RJ, Phifer DW. *Microsc Microanal* 2006;12:1310.
- [42] Lawrence D, Thompson K, Larson DJ. *Microsc Microanal* 2006;12(Suppl. 2):1740.
- [43] Cairney JM, Saxey DW, McGrouther D, Ringer SP. *Physica B* 2007;394:267.
- [44] Takahashi J, Kawakami K, Yamaguchi Y, Sugiyama M. *Ultramicroscopy* 2007;107:744.
- [45] Thompson K, Lawrence D, Larson DJ, Olson JD, Kelly TF, Gorman B. *Ultramicroscopy* 2007;107:131.
- [46] Pérez-Willard F, Wolde-Giorgis D, Al-Kassab T, López GA, Mittermeijer EJ, Kirchheim R, et al. *Micron* 2008;39:45.
- [47] Miller MK, Russel KF, Thompson K, Alvis R, Larson DJ. *Microsc Microanal* 2007;13:428.
- [48] Kelly TF, Camus PP, Larson DJ, Holzman LM, Bajikar SS. *Ultramicroscopy* 1996;62:29.
- [49] Kelly TF, Larson DJ. *Mater Charact* 2000;44:59.
- [50] Kelly TF, Gribb TT, Olson JD, Martens RL, Shepard JD, Wiener SA, et al. *Microsc Microanal* 2004;10:373.
- [51] Kelly TF, Larson DJ, Thompson K, Alvis RL, Bunton JH, Olson JD, et al. *Ann Rev Mater Res* 2007;37:681.
- [52] Kelly TF, Miller MK. *Rev Sci Instrum* 2007;78:031101-1.
- [53] Seidman DN. *Ann Rev Mater Res* 2007;37:127.
- [54] Hellman OC, Blatz du Rivage J, Seidman DN. *Ultramicroscopy* 2003;95:199.
- [55] Hellman OC, Vandenbroucke JA, Rüsing J, Isheim D, Seidman DN. *Microsc Microanal* 2000;6:437.
- [56] Fuller CB, Murray JL, Seidman DN. *Acta Mater* 2005;53:5401.
- [57] Marquis EA, Seidman DN, Asta M, Woodward C. *Acta Mater* 2006;54:119.
- [58] Isheim D, Gagliano MS, Fine ME, Seidman DN. *Acta Mater* 2006;54:841.
- [59] Marquis EA, Seidman DN, Asta M, Woodward C, Ozolins V. *Phys Rev Lett* 2003;91:036101-1.
- [60] Marquis EA. Ph.D. thesis. Northwestern University; 2002.
- [61] Marquis EA, Seidman DN. *Surf Inter Anal* 2004;36:559.
- [62] Perdew JP, Chevary JA, Vosko SH, Jackson KA, Pederson MR, Singh DJ, et al. *Phys Rev B* 1992;46:6671.
- [63] Hohenberg P, Kohn W. *Phys Rev* 1964;136:B864.
- [64] Kohn W, Sham LJ. *Phys Rev* 1965;140:A1133.
- [65] Kresse G, Furthmüller J. *Phys Rev B* 1996;54:11169.
- [66] Blöchl PE. *Phys Rev B* 1994;50:17953.
- [67] Kresse G, Joubert D. *Phys Rev B* 1999;59:1758.
- [68] Benedek R, van de Walle A, Gerstl SSA, Asta M, Seidman DN. *Phys Rev B* 2005;71:094201.
- [69] Kral MV. *Mater Lett* 2005;59:2271.
- [70] Miao WF, Laughlin DE. *Metall Mater Trans A* 2000;31A:361.
- [71] Beerl O, Dunand DC, Seidman DN. *Mater Sci Eng A* 2010;527:3501.
- [72] Haasen P. *Physical metallurgy*. New York: Press Syndicate of the University of Cambridge; 1996. p. 220.
- [73] Hardy HK. *J Inst Metals* 1951;79:321.
- [74] Hardy HK. *J Inst Metals* 1953–1954;82:236.
- [75] Silcock JM, Heal TJ, Hardy HK. *J Inst Metals* 1953–1954;82:239.
- [76] Boyd JD, Nicholson RB. *Acta Metall* 1971;19:1379.
- [77] Kurz W, Fisher DJ. *Fundamentals of solidification*. Zurich: Trans-Tech; 1992.
- [78] Knipling KE, Dunand DC, Seidman DN. *Z Metallkd* 2006;87:3.
- [79] Fujikawa SI, Takada Y. *Defect Diffus Forum* 1997;143–147:409.
- [80] Fujikawa SI, Hirano KI, Fukushima Y. *Metall Trans A* 1978;9A: 1811.